CrossMark

An improved buffer analysis technique for model-based 3D mineral potential mapping and its application

Nan Li [a,b,*], Leon Bagas [b,*], Xiaohui Li [c], Keyan Xiao [a], Ying Li [d], Lijuan Ying [a], Xianglong Song [a]

[a] MLR Laboratory of Metallogeny and Mineral Resource Assessment, Institute of Mineral Resources, Chinese Academy of Geological Sciences, Beijing 100037, China
[b] Centre for Exploration Targeting, The University of Western Australia, 35 Stirling Highway, Crawley, WA 6009, Australia
[c] School of Resources and Environmental Engineering, Hefei University of Technology, Hefei 230009, China
[d] Beijing Institute of Geological Survey, Beijing 100195, China

ARTICLE INFO

ABSTRACT

Buffer zones in bo\th two-dimensional (2D) and three-dimensional (3D) spaces are commonly used in prospectivity mapping. The method completes a modelling that starts with a real example and progresses to the development of a virtual model. This includes the consideration of lithological or structural contacts at depth, which is a theoretical concept based on extrapolation of data collected in the field, rather than an empirical observation of the feature based on physical samples. This contribution documents an improved buffer analysis method for the study of 3D-space that is implicit (rapid), precise (smooth) and based on triangulated characteristics, which can be used to construct influence domains of geological models. As traditional 2D GIS-based mineral potential mapping is gradually becoming limited with time, mineral potential mapping in three dimensions (3D) is increasingly becoming an important tool in finding concealed economic mineralization. This contribution documents an improved methodology of buffer analysis for prospectivity mapping processing mineralized favourable models rather than describing an advance in the geometry of surface rendering of "geological complexity". Measures used in this buffer analysis include the: (1) voxelization of geological objects (i.e. assigning numerical values of features on a regular cube in 3D-space); (2) revision of the 3D Euclidean distance transform and the calculation of signed distance field; (3) extracting surfaces from the field; and (4) construction of a buffer-surface based on a "discrete smooth interpolation" (DSI) algorithm. Furthermore, this contribution constructs 3D models using a buffer analysis algorithm and prospectivity mapping introduced here, which is based on real data from the Jiama Cu-polymetallic deposit in Tibet and Daye Fe deposit in the Hubei Province, China. This contribution also presents a comparison between voxel and irregular triangle models, which illustrate that irregular triangle mesh buffer analysis (ITB) can improve modelling techniques for GIS-based 3D mineral potential mapping. The outcome is an increase in the accuracy of prospectivity mapping.

© 2015 Elsevier B.V. All rights reserved.

1. Introduction

Model-based prospectivity studies integrate sets of data on minerals, maps or models with the aim to target potential mineral deposits from the regional to the camp scales. Traditionally, many model-based mineral potential mappings have been reported in two-dimensions (2D; e.g. Agterberg, 1970; Agterberg et al., 1990, 1993; Cargill and Clark, 1978; Bonham-Carter and Agterberg, 1989; Bonham-Carter, 1994; Cheng and Agterberg, 1999; Cheng et al., 1996; Cheng, 2007; Zhu, 1997; Wang, 1999; Singer, 1993, 2006; Singer and Menzie, 2010; Zhao, 2002; Zhao et al., 2003; Zhao, 2002,2007; Brown et al., 2000; Carranza, 2004; Carranza and Sadeghi, 2010; Zuo et al., 2009; Porwal and Hale, 2000; Porwal and Carranza, 2001; Tangestani and Moore, 2001; Porwal et al., 2006, 2010; Zhang et al., 2013). However, 2D GIS-based mineral potential mapping is limited, because mineralization are objects in three dimensions (3D), which is the main focus of this contribution.

A growing number of researchers are now applying 3D multi-maps (models) to predict the position of concealed ore-bodies for both deposit- and camp-scale using programmes such as Surpac™, Leapfrog, Micromine, GeoCAD and GeoModeller. Noteworthy examples are those of Chen et al. (2007)), Chen and Wang (2012), Wang et al. (2011), and Xiao et al. (2012) who apply 3D GIS tools for modelling and visualization of geological data in the 3D deposit-scale, without using quantitative methods. Yuan et al. (2014), Xiao et al. (2015) and Li et al. (2015) demonstrate both the value of 3D modelling and a quantitative data analysis workflow to improve exploration targeting of concealed deposits. Perrouty et al. (2012) built 3D models from data, including cross-sections, structural measurements and petrophysical records, and then completed 3D prospectivity mapping in the Ashanti Belt of

* Corresponding authors at: MLR Laboratory of Metallogeny and Mineral Resource Assessment, Institute of Mineral Resources, Chinese Academy of Geological Sciences, Beijing 100037, China.
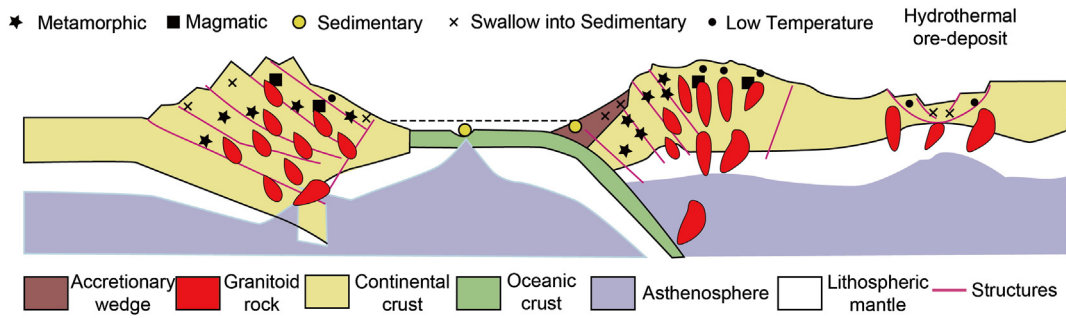E-mail addresses: Nan.Li@uwa.edu.au (N. Li), leon.bagas@uwa.edu.au (L. Bagas).

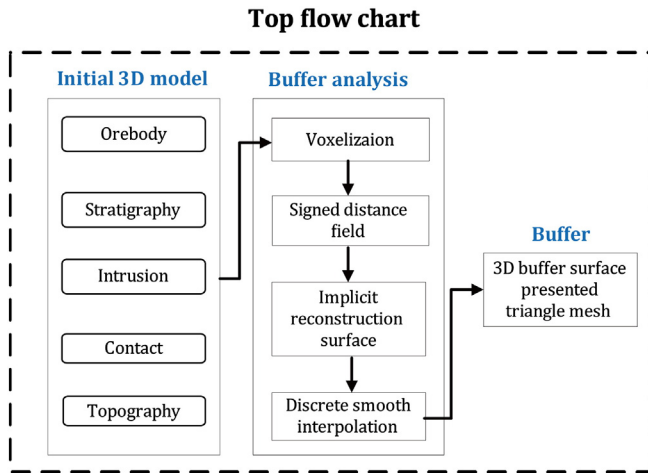**Fig. 1.** Tectonic settings for different types of hydrothermal systems (modified after Chen, 2010).

Fig. 2. A flow chart summarizing the steps used for triangle mesh buffer analysis in potential mining.

southwest Ghana, Africa (Perrouty et al., 2014). Mao et al. (2012) discussed to apply morphological analysis of 3D geological features to 3D mineral prospectivity mapping. Malehmir et al. (2009) and Lü et al. (2013) demonstrate how 3D modelling provides ways of exploring for sub-surface geometries using known deposits to develop spatial correlations with mineralization and subsequently applying these principles as guides for mineral exploration.

Porwal and Carranza (2015) have outlined three critical parts necessary for model-based mineral potential mapping, which are: (i) research for a conceptual geological and metallogenic model; (ii) collection of data and construction models (maps); and (iii) integration of representative predictor models that are output to a target. Principally, in the second step above, it is important for GIS-based mineral potential mapping to identify and construct consistent and representative models related to potential deposits. Skarn and hydrothermal vein-type mineralization deposits, for example, require a source, a conduit for mineralized fluids to flow through to physical traps and chemical scrubbers for such deposits to develop (Fig. 1) (Chen, 2010); the combinations of each of these criteria are necessary to define potential areas or domains for mineralization (Wang et al., 2014a, 2014b, 2014c, 2015a, 2015b). In addition, as illustrated in Fig. 1, the surrounding area of known deposits, which is termed "influence domain", includes favourable host rocks and structures (, and has a good mineral potential for hydrothermal ore-deposit. Furthermore, the type of "influence domain" can be closely exemplified using buffer analysis as part of GIS-based prospectivity studies. A current critical limitation, however, is that "influence domain" models cannot be built directly using real data (samples) in most instances, because this type of domain is regarded as a kind of virtual object centred on structures or the interface of rock types.

Computer implementation of buffer analysis in 3D is much more difficult than in 2D. The significant difficulty is that 3D-buffer analysis has to deal with a large number of calculations involving geometry intersections resulting in extremely approximate body's boundary representations (Wu et al., 1999; Lu and Wang, 2012). Some researchers use voxel-model (block-model) buffers in order to avoid these complex calculations and inherent inaccuracy (e.g. Wu, 1997; Li et al., 2005). Li et al. (2005) proposed an efficient algorithm for 3D raster buffer-generation based on iso-surface propagation, however there are two problems with this procedure. One is the lack of precision (refer to Figs. 18 and 19), because volume does not clearly present the shape details of geological objects as accurately as triangular surfaces do. Obviously, the volume of cubes or other polyhedrons are limited by the size of polyhedrons and complexity of a geological object. The other is redundancy, as discussed in Section 4.3.1. For example, a corner of a surface can be represented by a few triangles as well as tens of cubes. Furthermore, significantly more voxels are needed to more accurately
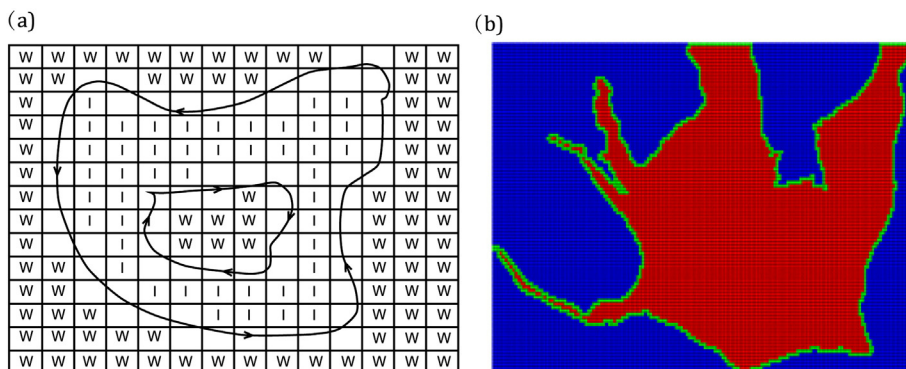

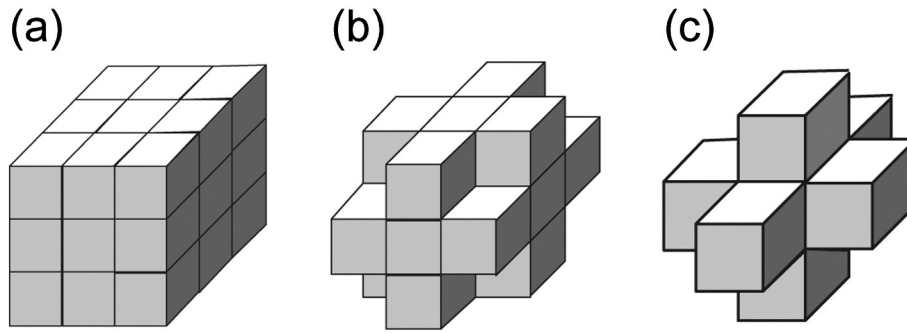**Fig. 3.** Adjacent relationship of the FloodFill algorithm in 2D-space.

Fig. 4. Adjacent relationship of the FloodFill algorithm in 3D-space: (a) 26-advacency; (b) 18-advacency; and (c) 6-adjacency.

represent an object resulting in difficulties due to computer memory limitations. Other researchers have introduced the idea of parallel computing as a tool in prospectivity studies (e.g. Yuan et al., 2014). This method uses the "computer unified device architecture" (CUDA) platform developed by nVIDIA and improves the efficiency of computation significantly, but it necessitates the incorporation of additional computer hardware.

As mentioned above, construction of a geological model is a critical part of model-based prospectivity mapping, and 3D buffer analysis is an important way to develop geological models. Thus, this paper discussed this imperfect issue and proposes an improved method for buffer-analysis-modelling with precision. The result is improved model-based prospectivity mapping in both target and quantification.

2. The essence of irregular triangle-mesh buffer analysis

In this contribution, we focus on the triangle mesh buffer analysis of surface models for geological objects. As defined by Wu and Lü (2001), the aim of buffer analysis is to guarantee the "same buffer distance" from a geological feature everywhere within a model and to refine it in a process of calculation. The same buffer distance means any point that exists on a geological surface that has the same minimum distance to its buffer surface. In 2D-space, GIS uses the intersection calculation of segments to satisfy this constraint. Obviously, an algorithm in 3D-space must carry out a number of intersections of triangles to satisfy this requirment, but this is almost an impossible task to limited resources of computer (Wu and Lü, 2001; Zhang and Wen, 2006).
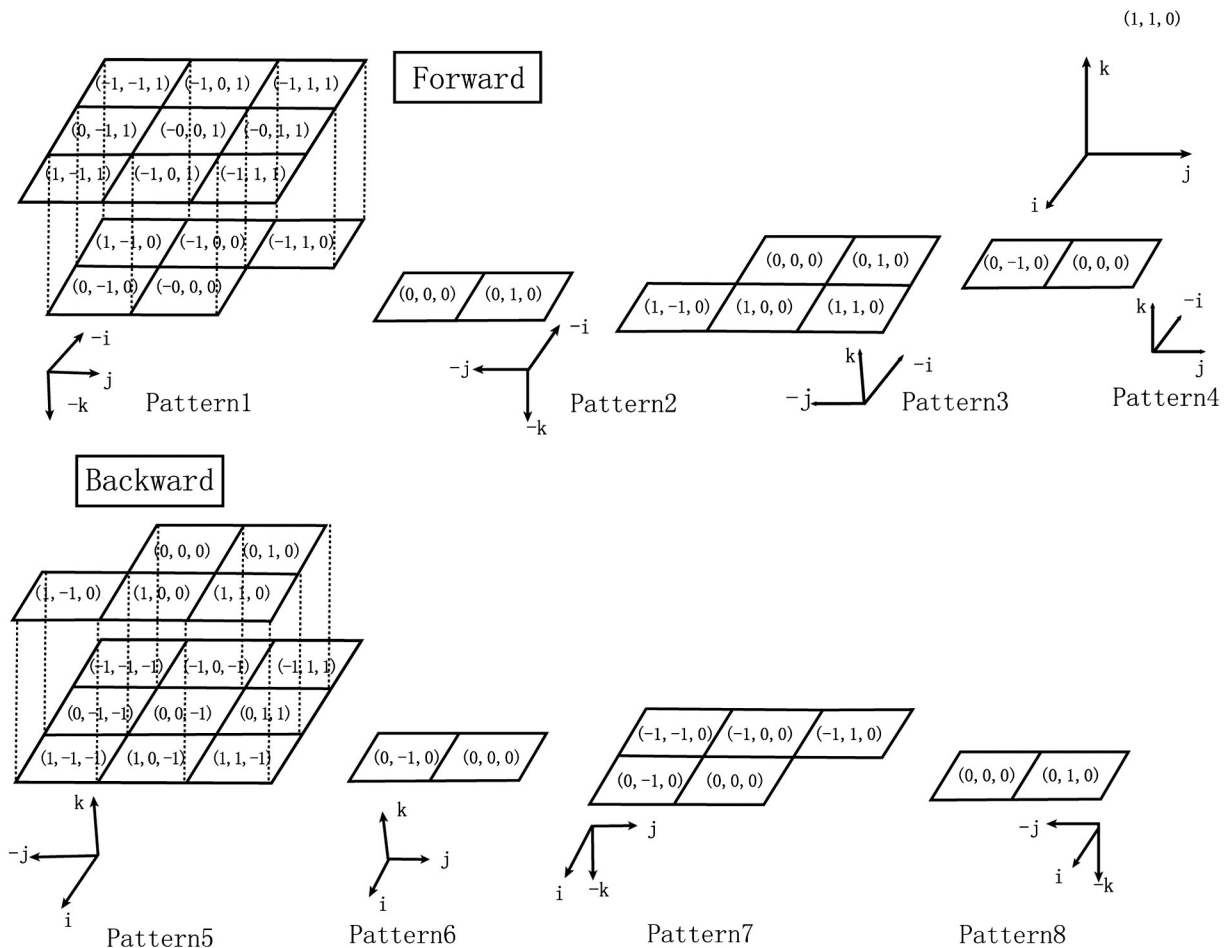

Fig. 5. Flow chart of signed Euclidean distance transformation (revised by Lin and Wang, 2003).
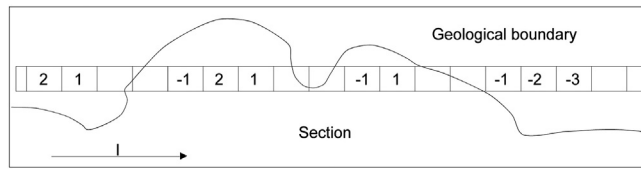
Fig. 6. Example of a section resulting from transformation, where word 'I' is an integer number.
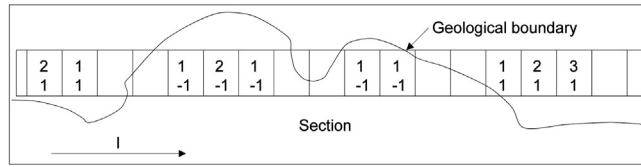

Fig. 7. Improved SEDT for Buffer Analysis, where word 'I' is an integer number.

The intersection of triangles in 3D-space is totally different with the intersection of segments in 2D-space, because 3D-space requires the intersection of two planes essentially. In 3D analyses, the intersection between any two triangles includes the calculation of the distances between edges and triangle, splitting of two intersected triangles, re-triangulation, and reconstruction topological surface that include intersected triangles (Wu et al., 1999; Lu and Wang, 2012). Each step in this process will affect the complexity and stability of a buffer analysis algorithm. As such, the topological reconstructions in 3D are no easy tasks (Houlding, 1994; Hou and Wu, 2002; Zlatanova et al., 2004; Schneider and Behr, 2006; Ellul and Haklay, 2006; Li et al., 2012).

It is therefore evident that we need to modify traditional techniques used in 2D constructions and continue to develop tools for 3D surface constructions. There are currently two kinds of surface reconstruction available, which are known as "explicit" and "implicit" methods in 3D graphics. Explicit methods directly create a surface

representation from the input point set by interaction. The result is usually a Delaunay-triangulated surface (Edelsbrunner and Mucke, 1994; Bajaj et al., 1995; Amenta et al., 2001). In contrast, the implicit methods reconstruct a surface from an isovalue of implicit functions including "marching tetrahedron" and "cubes" (Lorenesen and Cline, 1987; Treece, 1999). Hoppe et al. (1992) first introduced surface reconstruction using a signed distance field in their pioneering paper. For instance, we can construct a reference surface automatically, the algorithm can implicitly create a surface of buffer analysis automatically. As indicated in the introduction above, buffer analysis has a close relationship with distances. Thus, the reference surface can be extracted using the "marching cubes" (or "tetrahedron") method of Lorenesen and Cline (1987) and Treece (1999) based on the signed Euclidean distance field (Danielsson, 1980; Lin and Wang, 2003). Lajaunie et al. (1997) and Calcagno et al. (2008) applied interpolation to restructure 2D and 3D geological models that can be seen as geological prior model by implicit method for
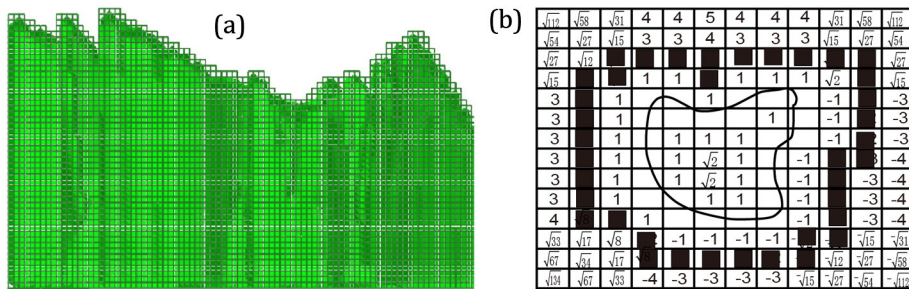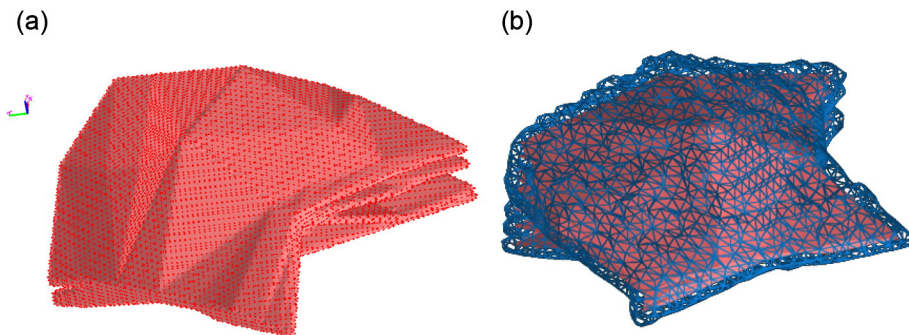

Fig. 8. Signed Euclidean distance field in 3D.

Fig. 9. DSI "smooth" and "equality": (a) inserted central points (free points); and (b) smooth surface by roughness function.
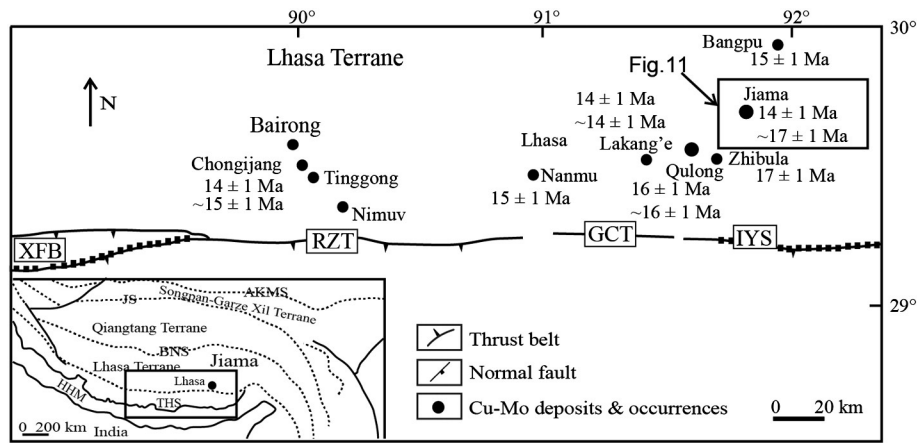
Fig. 10. Regional geological map showing the major porphyry Cu deposits in the Gangdese belt of southern Tibet. The ages of the deposits are based on molybdenite Re–Os dates. The inset shows the major tectonic units of the Tibetan Plateau (Hou et al., 2011; Ying et al., 2014).

geophysical inversion. Obviously, implicit method has several advantages compared to explicit method on buffer modelling. But there is a important problem to need to be solved. That is size of triangle. Obviously, size of triangle depends on size of voxel widely in implicit method. Thus, the final measure, we used "discrete smooth interpolation" (DSI) algorithm(Mallet, 1997, 2003).
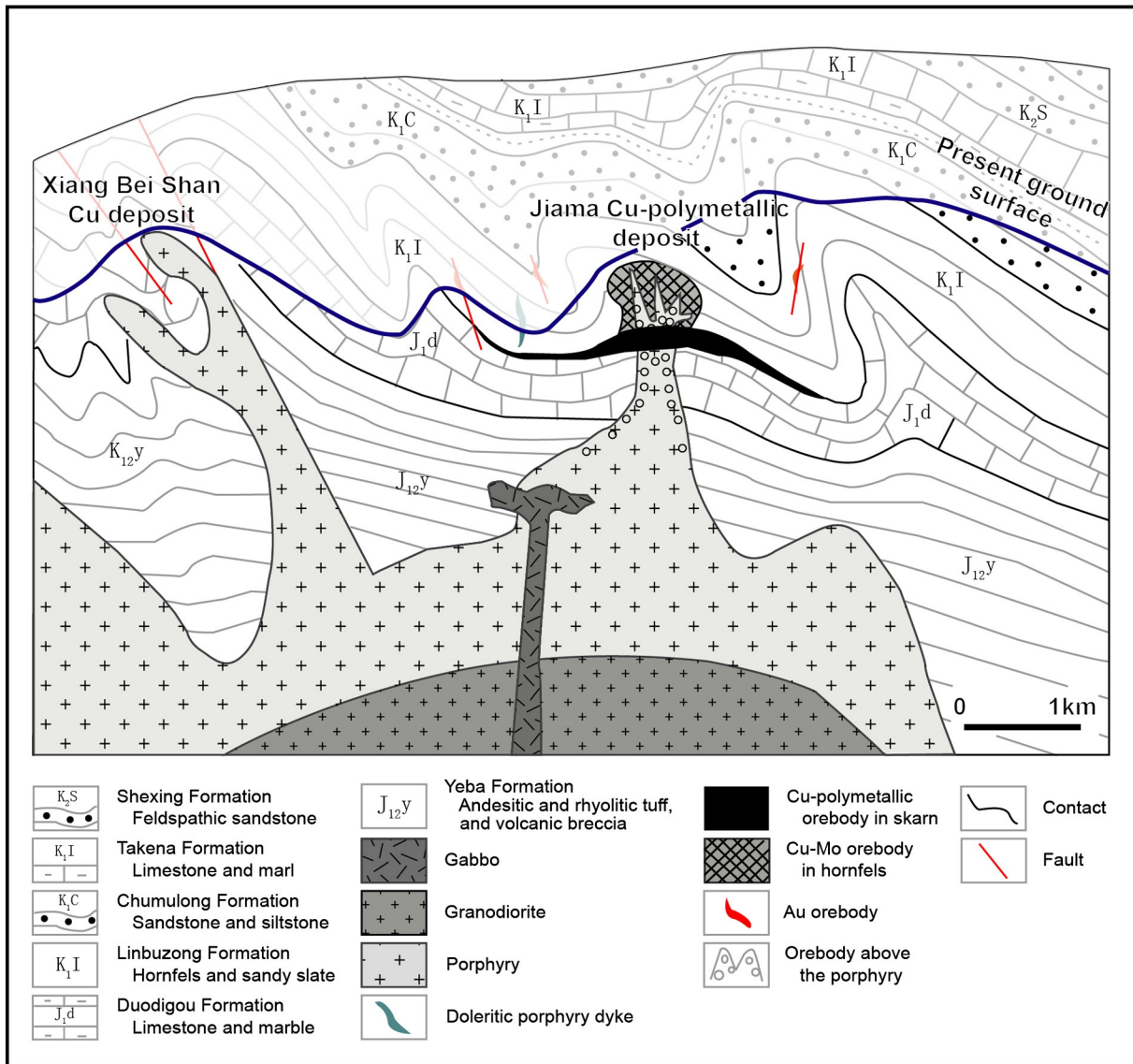

Fig. 11. Cross-sectional sketch of the Jiama Cu-polymetallic hydrothermal deposit in Tibet (modified after Tang et al., 2010).
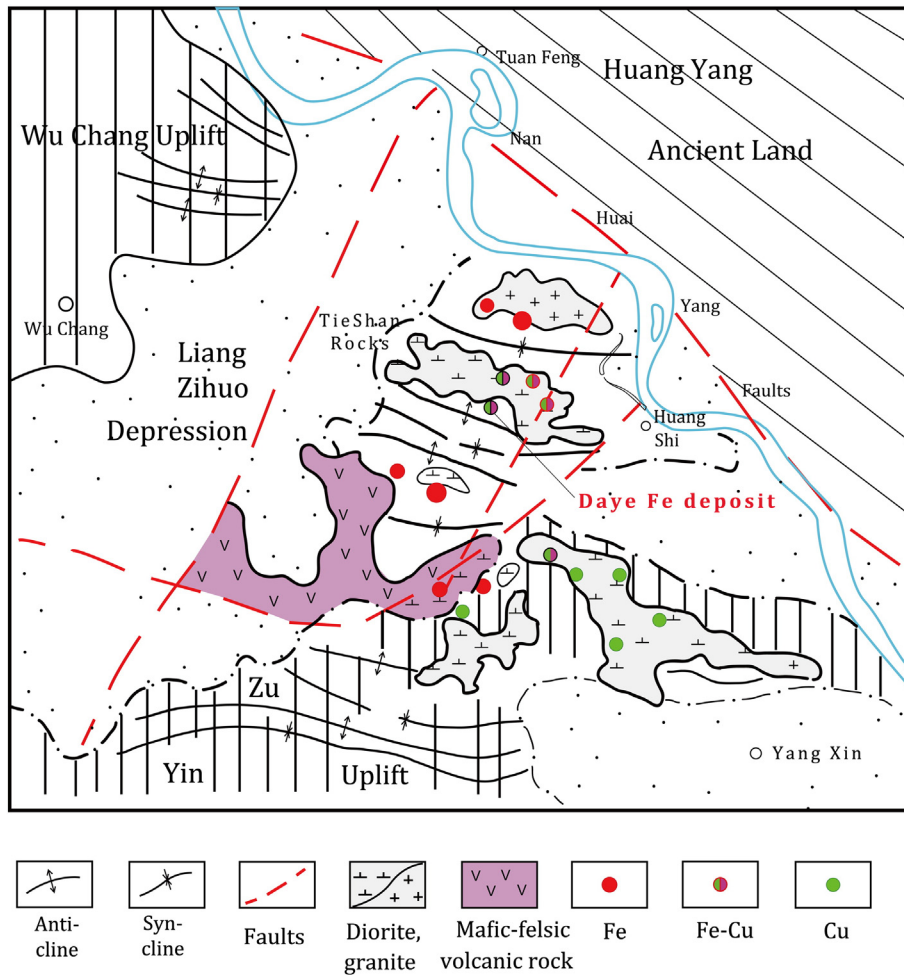
Fig. 12. Regional geological map showing the location of the Daye Fe deposit in the western part of the Middle-Lower Yangtze Cu–Fe metallogenic belt of south eastern China.

The DSI algorithm includes the construction of a reference surface using the way of interaction, and it implicitly calculates based on the "global roughness" formula (Mallet, 1997, 2003). In this paper, we inserted center of each triangle into reference surface. Thus, the points, P, on reference surface are defined to fixed points and center points, P_c, are seen as free points.

The main aim of the irregular triangle mesh-buffer analysis of surface models for geological objects is to form a construction-surface based on the distance field. This process involves: (i) voxelization of geological objects; (ii) revision of the 3D Euclidean distance transform; (iii) calculating the signed distance field; (iv) extracting surfaces from the field; and (v) smoothing buffer surface based on the DSI algorithm. The methodology: (a) guarantees the accuracy of the buffer analysis, which means that the surface of a buffer analysis should pass through project points calculated by nodes on original geological object; (b) employs the Euclidean distance transform (Danielsson, 1980; Ye, 1988; Lin and Wang, 2003) and marching cubes (or tetrahedron of Lorenesen and Cline, 1987; Treece, 1999) algorithms; (c) reduces the intersection of triangles, re-triangulation and topology reconstruction; and (d) improves efficiency and stability. In addition, the triangle mesh buffer analysis will decrease calculation complexity in quantitative assessment. Fig. 2 is a flow chart of summarizing the steps in triangle-mesh buffer analysis in potential mining.

The following section discusses and summarizes the workflow for an algorithm of tri-buffer analysis involving: (1) construction of 3D GIS-layers to represent mineralization; (2) 3D tri-buffer analysis calculation used for extrapolation; and (3) tri-buffer using a boundary-representation model. Especially, (2) and (3) are major content of this paper.

3. Implementation of the irregular triangle mesh buffer analysis

The construction of the buffer surface includes four steps, as shown in Fig. 2, and its implementation is discussed below.

3.1. Voxelization of surface model of geological objects

The first step in the method developed here is voxelization, which is a process of assigning numerical values of features on a voxel in 3D-space as described by Li et al. (2013). This is an improving method that extends the process of "Flood Fill" introduced by Feito et al. (1995), which is a process that extends from a 2D-space to a 3D-space (as shown in Figs. 3 and 4). Using the improving method, voxelization is a process that models the surfaces of geological objects using volume and three kinds of cubes (i.e. inner, outer and border cubes) as shown as Figs. 3 and 4.

The size of each cube in this technique is the same, and the number value of the size of the object is equal to the buffer distance set by the researcher. In other words, length, width and height of each voxel are the same and equal to the buffer distance. On passing, there are two situations that need to be explained. The first is when the buffer distance is "too small". In this case, the criteria for being "small" is when the distance (millimetre, metre, or kilometre) is less than a specific size threshold of voxels above which result in
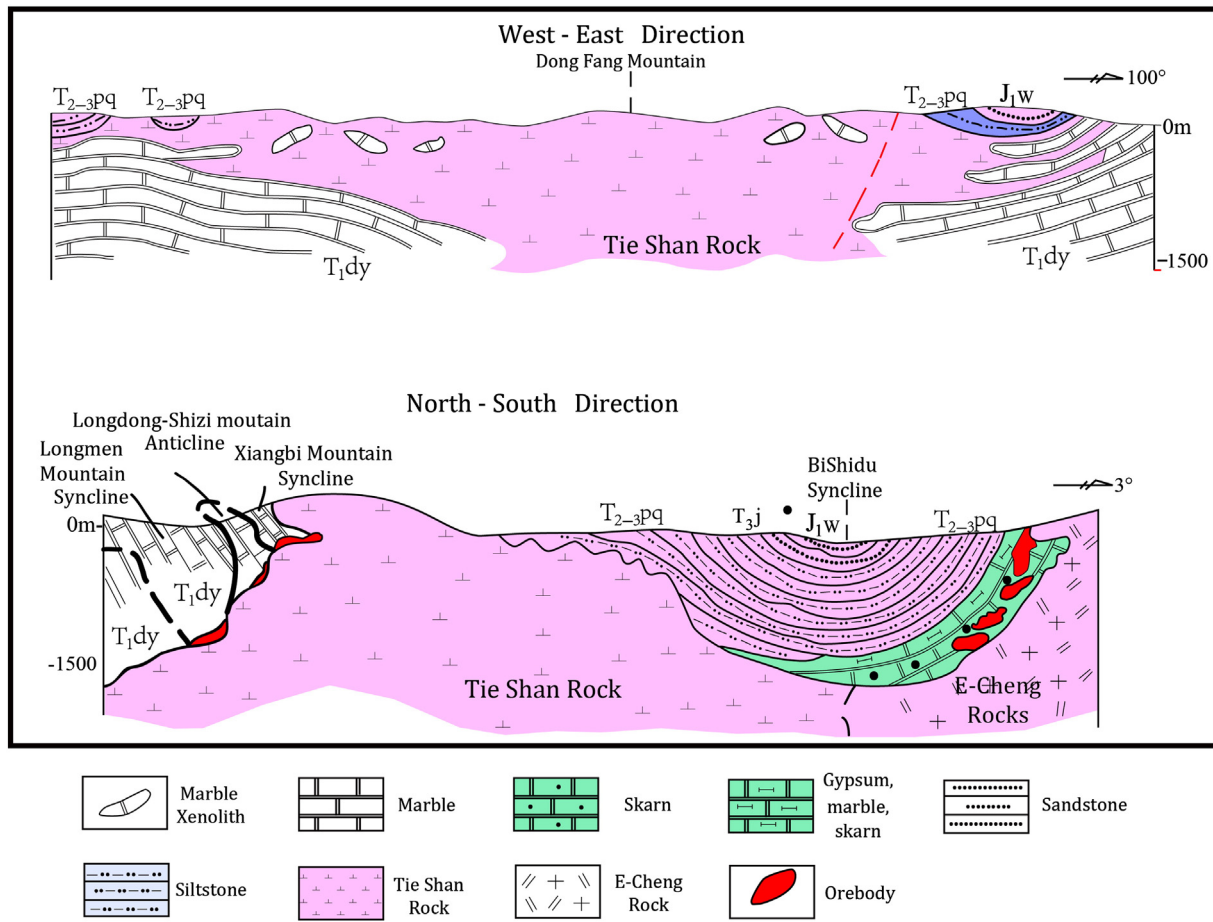
Fig. 13. Cross-sectional sketch of the Daye Fe mineralization in the Hubei Province.

computational difficulties or memory exhausted. The second situation is when the buffer distance is "too large" resulting in an inadequate number of voxels that is necessary to accurately define a buffer surface.

3.2. Signed Euclidean distance transformation

The signed Euclidean distance transformation is an important research field used in GIS and digital image processing. Danielsson (1980) first applied the process to deal with 2D image transformation from black and white to grey-scale images. Lin and Wang (2003) then extended it to the 3D-space rapidly constructing signed distance fields. However, the signed Euclidean distance transformation is not completely suitable for buffer analysis with the resultant transformation being classified as "characteristic" and "non-characteristic" cubes (Li et al., 2013). This contribution improves the method of Lin and Wang (2003) making it suitable for buffer analysis of 3D objects.

The essence of 3D-signed Euclidean distance transformation is the communication process involving distance information (Lin and Wang, 2003). The process includes what are termed "forward" and "backward" transformations in Fig. 5 (modified from Lin and Wang, 2003). In addition, the transformation illustrated in Fig. 5 is a classic Euclidean distance transformation, with the result shown in Fig. 6

Table 1
Data sets.

| Data set type	Scale	Description of the data	Source
Details of original multi-type data in Jiama deposit			
Bore holes and trenches	–	218 bore holes and 10 trenches; *the average bore hole spacing* is 100 m; *bore hole depths* range from 3800 to 5400; *bore the core sample length* ranges from 0.8 m to 3 m; *the average trench spacing* 100 m; *trench depth* ranges from 10 m to 25 m; *trench' logging length* ranges from 6.6 m to 66.4 m.	Tang et al. (2009)
Cross sections	–	26 exploration cross-sections and *their spacing* is almost 100 m;	Tang et al. (2009)
Geological map	1:2000	1 map covered the whole deposit	Tang et al. (2009)
Topographic maps	1:2000	1 map covered the whole deposit	Tang et al. (2009)
Details of original multi-type data in Daye deposit			
Bore holes and trenches	–	42 bore holes and 34 trenches; *the average bore hole spacing* is 80 m; *bore hole depths* range from −1090 m to 218 m; *bore the core sample length* ranges from 0.17 m to 9.90 m; *the average trench spacing* 80 m; *trench the core sample length* ranges from 0.75 m to 3.00 m;	Liu and Luo. (2008)
Cross sections	–	17 exploration cross-sections and *their spacing* is almost 100 m;	Liu and Luo. (2008)
Geological map	1:2000	1 map covered the whole deposit	Liu and Luo. (2008)
Topographic maps	1:2000	1 map covered the whole deposit	Liu and Luo. (2008)
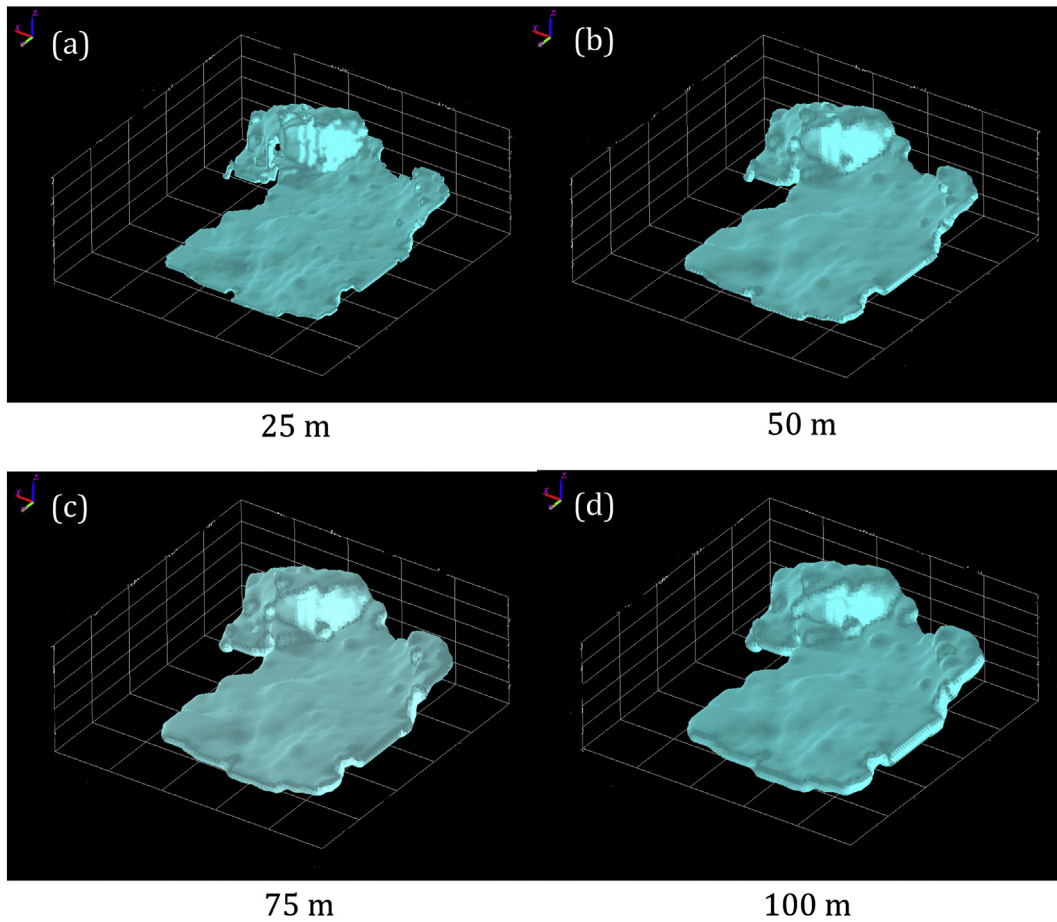
Fig. 14. Contact buffers at the Jiama polymetallogenic deposit.

(where the integer is the minimum distance from non-characteristic to characteristic cubes). The shape of the geological boundary shown in Fig. 6 is not symmetrical between the positive or negative distances below the boundary. This asymmetry is here addressed by taking classic rules and geometry topology into account.

As discussed in Section 3.1, cubes are termed "inner", "outer" and "border" cubes (Feito et al., 1995). This contribution improves classic transformation by adding a binary mark that records the relationship between a cube and the boundary of original surface model of geological objects. Using this method, inner voxels are given a negative 1 and the outer cubes are a given a positive 1, thus cancelling the negative sign of the integer in Fig. 6. Finally, the distance field for Euclidean transformations is here satisfied with the topology of the geological surface while preserving the advantages of classic transformations (as shown in Fig. 7). Furthermore, as the size of each cube is equal to the buffer distance (except for the two exceptional cases mentioned in Section 3.1), cubes with a distance of 2 will be preserved. The effectiveness of the distance field is shown illustrated in Fig. 8.

The final step is to calculate the real distance field to replace the integer values. This is a very simple process of linear complexity involving the procedures described in this Section and Section 3.1, as summarised in Figs. 6 and 7, because all of the points needed to calculate the real distance are the same as the distance from the characteristic cube.

3.3. Construction of a buffer surface

The "marching cubes" (MC) or "tetrahedron" (MT) algorithm is a reasonable and efficient implicit method of restructuring the surface from the distance field (refer to Section 3.2) for DSI. This surface is an iso-surface where the isovalue is equal to the buffer distance. The MT

is a more reliable method, because it is without ambiguity compared to the "marching cubes" (MC) method. On the basis of the signed distance field and MT, a group of surfaces will be extracted, where a positive distance corresponds to an outer buffer zone and a negative distance corresponds to an inner buffer zone.

3.4. Construction of a "smooth buffer surface"

The DSI algorithm was originally proposed by Mallet (1997, 2003). The algorithm has gradually been modified into a set of functional computer-aided design methods, such as in GOCAD™. The essence of the algorithm consists of the construction of a reference surface by the way of interaction, and it is implicitly smoothed by the roughness functions, fixed points and free points on reference surface.

In this section, we use the DSI method to form a smooth buffer surface (S) constructed using Section 3.3. All of the points (P) on S are defined as a fixed point set, then a central point was inserted to each triangle on S and each triangle on S was re-triangulate where all of the inserted points (P′) are defined as a free point set. Finally, the method for constructing a smooth buffer surface by roughness to set P′ using the DSI algorithm is shown in Fig. 9.

3.5. Incorporation into 3D GIS

In this paper, we use the Drawing Exchanged Format (DXF) with ASCII to make our method flexible and user-friendly. As shown in Fig. 1, initial 3D models will be imported and boundary representations of buffer analysis exported using DXF files, and finally, they will be incorporated into the 3D GIS platform for simulating mineral potential mapping using mathematical models.
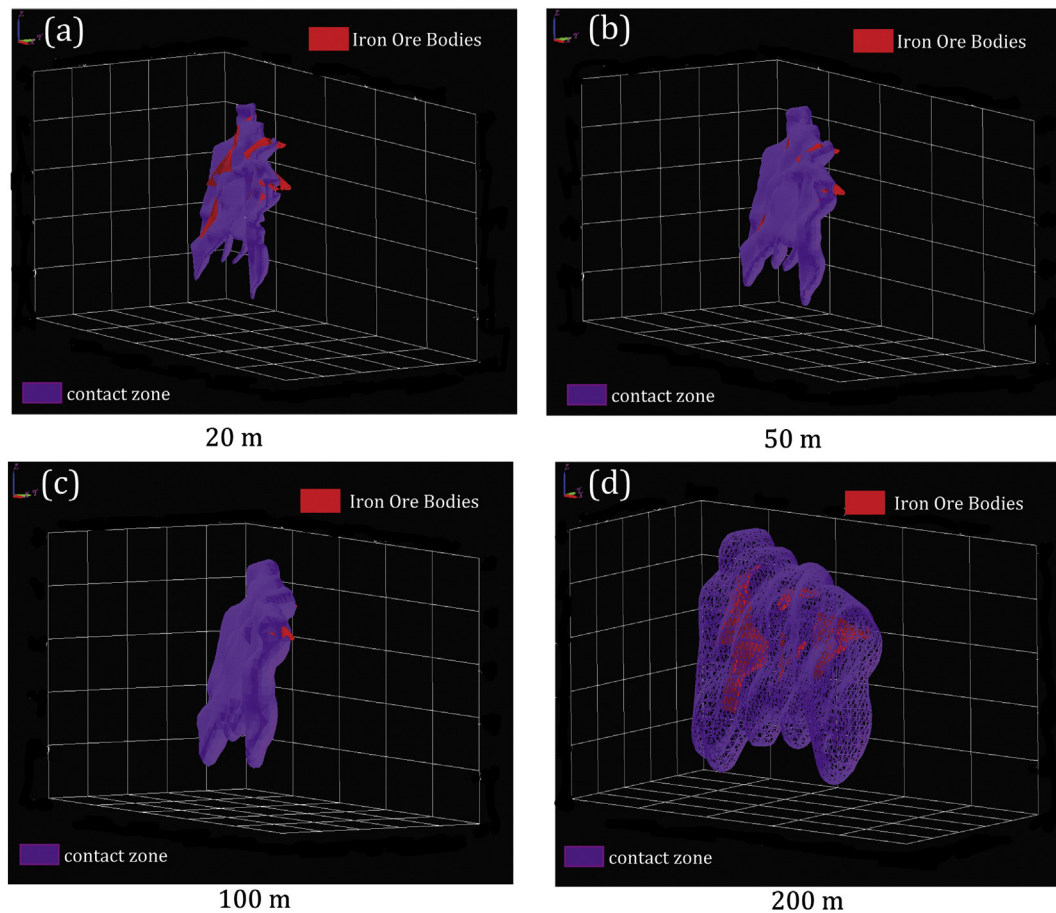
Fig. 15. Interface buffers at the Daye Fe deposit.

4. Application of 3D "irregular triangle-buffer analysis" on 3D mineral potential mapping at deposit-scale

The buffer analysis method presented here is implicit, precise and has triangulated characteristics. The buffer analysis is used to construct domains of influence for geological bodies, as mentioned in Section 1. In the case of the Jiama Cu-polymetallic deposit, this can include features such as lithological contacts, faults and the rock types surrounding magmatic hydrothermal mineral deposits included in 3D mineral-potential mapping studies.

The following presents a group of contrastive analyses between irregular triangle mesh buffers and raster buffer zones. This is done using 3D visualization effect, goodness of fit, and weights-of-evidence classification by using 3D models for two different study areas. In this section, the 3D models used are from the Jiama Cu-polymetallic deposit in Tibet (Tang et al., 2010) and Daye Fe deposit in the Hubei Province (Liu and Luo, 2008).

4.1. Study district

4.1.1. Geological setting of the Jiama polymetallogenic deposit

The Gangdese porphyry-Cu belt is located in the eastern part of a 1000-km long tectonic–magmatic belt in southern Tibet (marked by the rectangle area in the inset on Fig. 10). The belt is highly prospective for Cu-polymetallic deposits, which contain resources of more than 18 Mt of Cu (Hou et al., 2009; Hou et al., 2011). The Middle Miocene Jiama porphyry–skarn deposit in the belt contains 4.6 Mt of Cu with an average grade of 0.44%, 380 Kt of Mo with a grade of 0.036%, and 2.995 Moz of Au with a grade of 0.21 ppm (Ying et al., 2014). The rocks at Jiama consists of limestone and marble assigned to the Late

Jurassic Duodigou Formation (J3d), and sandstone, siltstone and shale assigned to the overlying Early Cretaceous Linbuzong Formation (K1l) (Fig. 4). The main types of mineralization at Jiama are hornfels- and skarn-types hosted by sandy slate and hornfels of the Linbuzong Formation and marble and limestone of the Duodigou Formation (Tang et al., 2010, 2011; Zheng, 2012). Obviously, the hornfels-type of mineralization is hosted by hornfels that form favourable traps for magmatic-hydrothermal mineralization in the area, and the skarn-type mineralization is hosted by interlayered hornfels and marble (Fig. 11).

4.1.2. Geological setting of the Daye deposit

The Daye Fe deposit is located in the western part of the Middle-Lower Yangtze Cu–Fe metallogenic belt. The Tieshan Complex hosts the Daye Fe deposit and is characterized by Jurassic to Cretaceous (Yanshanian) multi-stage dioritic–granodioritic plutons. The complex trends ESE, is 24 km long and approximately 6 km wide, and has an outcrop area of about 120 km^2.

The rocks at Daye include quartz diorite, biotite-diopside diorite, monzodiorite, quartz-bearing diorite porphyry, and minor dykes of diorite porphyry, lamprophyre and dolerite. The quartz-bearing diorite and biotite–diopside diorite are closely associated with iron mineralization (Fig. 12).

The ESE-trending zone in the middle segment of the southern margin of the Tieshan pluton is a composite zone, which is not only an intrusive contact but also an ESE-trending fault zone. Tectonic activity along this zone advanced through all the ore-forming stages displaying multi-stage and obvious inheritance patterns resulting from compression, extension and shearing. The ESE-trending zone commonly dips southwards and controls the shape, occurrence and distribution of the orebodies at the Tieshan Fe deposit (Fig. 13).
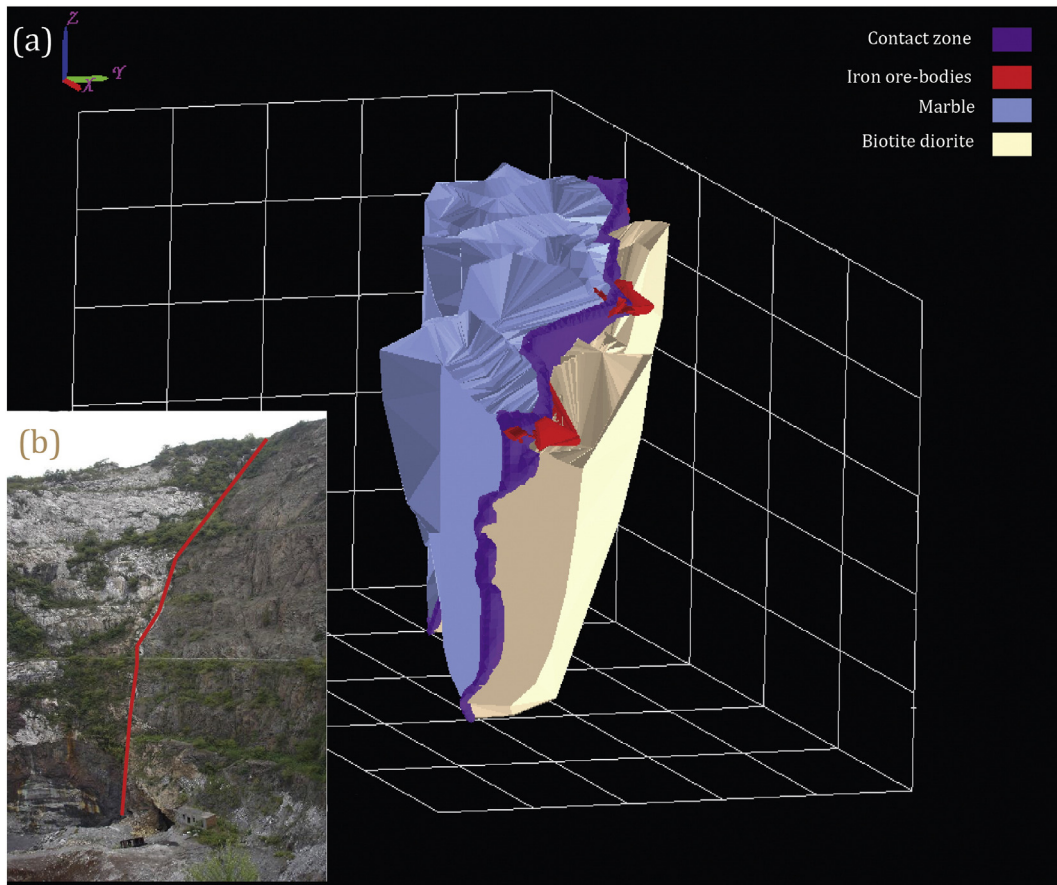
Fig. 16. Models of ore-bodies and their surrounding rocks at the Daye Fe deposit displaying: (a) 3D models; and (b) a photograph.

4.1.3. Data sets

In addition to topographic data, exploration datasets used in 3D-modelling at the Jiama Cu-polymetallic deposit include cross-sections, bore holes, and geological maps at 1:2000-scale sourced from Tang et al. (2009). Similar data has been compiled for Daye Fe deposit in the Hubei Province from Liu and Luo. (2008; Table 1).

4.2. Influence domains of geological objects

4.2.1. Influence domains (zone) of interface

As discussed in Sections 4.1.1 and 4.1.2, the contact between two units and their adjacent zones are critical to the mineralization at Jiama and Daye (Tang et al., 2010). Essentially, this type of zonation is a virtual geological spatial object that exists in researcher's reasoning that cannot be constructed when simply collecting data and constructing models (Porwal and Carranza, 2015). Buffer analysis of the interface between the Duodigou and Linbuzong formations at Jiama using the GIS-based 3D prospectivity map by Xiao et al. (2015) is here used as

an example by calculating buffers that are 25, 50, 75 and 200 m wide (Fig. 14a-d). Furthermore, the contact between marble and diorite at Tieshan is a critical ore-controlling structure containing mineralization. The contact has thus been presented as another example showing buffers that are calculated at widths of 20, 50, 100 and 200 m (Fig. 15). In addition, mineralized structures such as faults can play a crucial role as conduits for hydrothermal fluids, with many examples of deposits hosted by deep-seated and long faults. Buffering of mineralized faults can be used to quantify a relationship between faults and mineralization (as shown as Figs. 14 and 15).

4.2.2. Ore-bodies dependency of contact zone

As Section 4.1 and Fig. 13 show at Daye, quartz-bearing diorite and biotite–diopside diorite are closely associated with iron mineralization and the main ESE-trending structural zone. The structure commonly dips southward and controls the shape, occurrence and distribution of the orebodies at the Tieshan Fe deposit. Consequently, models were constructed of the ore-bodies and their surrounding rocks in Fig. 16(a), based on exploration reports for the Daye Fe deposit (Liu

Table 2
Proportion of ore-body models that intersect contact zones.

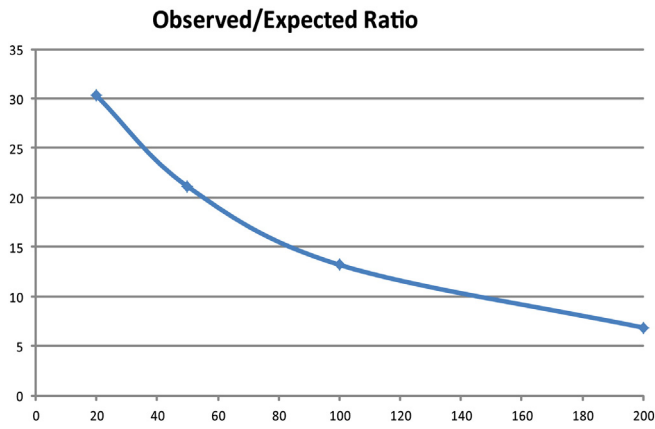| Buffer (1)	Number of voxels in each buffer pathway (2)	Cumulative number of voxels in buffer pathway (3)	Proportion of voxels in cumulative buffer pathway (4)	Number of ore-body voxels in each buffer pathway (5)	Cumulative number of ore-body voxels in each buffer pathway (6)	Observed number of voxels in the cumulative buffer pathway (7)	Expected number of voxels in the cumulative buffer pathway (8)	Observed/expected ratio (9)
0–20 m	6631	6631	0.026727773	1655	1655	1655	54.60483929	30.308669
20–50 m	4073	10,704	0.043144937	206	1861	1861	88.14510629	21.11291345
50–100 m	7703	18,407	0.074193652	139	2000	2000	151.5776319	13.19455896
100–200 m	17,807	36,214	0.145968867	43	2043	2043	298.2143945	6.850775943
>100 m		248,094	1		2043	2043	2043	1

Observed/Expected Ratio

Fig. 17. Proportion between ore-bodies and the pathway along contact zones.

and Luo, 2008). As can be seen from Section 4.3.1 and Fig. 16, the method allows researchers to build contact zones based on the interface surface. Unfortunately, however, only one contact zone can be put into the next step of integration and output as a target. To deal with this problem, a ratio was calculated between the observed number of voxels in the cumulative buffer and the expected number of voxels in the cumulative buffer. The ratio is positive for the ore-bodies controlled by contact zones, and the higher the value the higher the dependence is. To calculate the ratio, a voxel models were built with $50 \times 50 \times 25$ m buffers overlapping the ore-bodies or buffers (contact zones) with the voxel model calculated (Table 2 and Fig. 17).

Table 2 and Fig. 17 show that there are positive associations between different contact zones and ore-bodies and the value of the observed or expected ratio of the maximum 20 m buffer. Thus, the 20 m buffer is regarded as being more suitable for integration and output to target for mineral potential mapping.

4.3. Contrastive analysis

In this section, the buffer analysis visualization "goodness of fit" and targets are used for Jiama or Daye to explain how the triangle mesh buffer analysis introduced in this contribution is more efficient than raster buffer analysis.

4.3.1. Contrastive analysis of 3D geometry

Fig. 18 presents two separate 3D images for the surrounding rock of the Daye Fe deposit. The figure is produced using a 20 m raster buffer and triangles mesh with the same buffer distance (Fig. 18a, b where the size of the voxel is $20 \times 20 \times 20$ m), and Fig. 18c represents a combination of Fig. 18a and b. As can be seen, green colour zone envelopes a blue zone, which means that the geometry of the triangle mesh surface is more precise than for the raster surface.

4.3.2. Mean distance difference of theoretical buffers

The second contrastive analysis is known as "mean distance difference". This analysis involves calculating the mean distance difference between the buffer surface and the "initial surface" (S) of objects such as a geological body. Lin and Wang (2003) describe the procedure involved in quickly calculating the minimum distance from a point to the B-Rep surface. The surfaces shown in Fig. 18(a, b) are used to demonstrate the difference between surfaces represented by triangle- and voxel-buffers. In this example, a group of points are defined on the "initial surface" following the rule that a point (p) forming the centre of a triangle (T) is part of the "initial surface". The results are the intersections p_1 and p_2 on the surfaces showed in Fig. 18a, b with distances d_1 and d_2. Finally, the difference between the means of d_1 and d_2 are compared. The result is shown in Table 3 and Fig. 19. Obviously, the triangle

mesh buffer is more exact than the voxel buffer, because the triangle buffer surface is calculated based on algorithms pertaining to the iso-surface while the voxel-buffer has to respect the size of a voxel.

4.3.3. Comparison between the two buffer analysis methods in the mineral potential of Jiama

In this section, the extent of the difference in the integration of representative predictor models are compared and output to a target by using triangle- and voxel-buffers.

Using the statistics and analysis presented in Section 4.2.2, the buffer width of 75 m was chosen for the contact between the Linbuzong and Duodigou formations and integrated as a mineralized structure. Different integrations based on triangle-buffer (Fig. 20a) and the 75 m voxel-buffer (Fig. 20b) are presented in the prospectivity map. Xiao et al. (2015) describe mineral potential mapping using the 75 m tri-buffers, which have been adopted here for mineralized structures and parameters, but not for the contact zone.
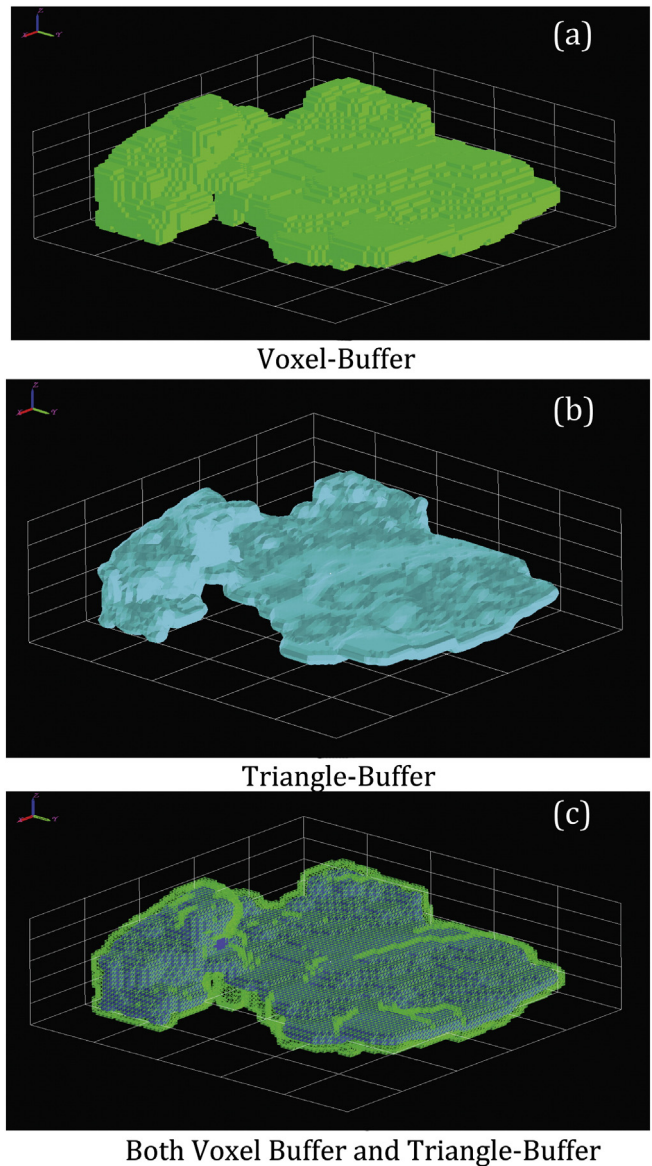

Voxel-Buffer

Triangle-Buffer

Both Voxel Buffer and Triangle-Buffer

Fig. 18. Three-dimensional models for rocks at the Daye Fe deposit showing: (a) 75 m raster buffer; (b) 75 m triangle mesh buffer; and (c) 75 m tri-contact zone with transparent and frame-style voxel-contact zone.

Table 3
Mean distance difference.

Buffer (m)	20 m	40 m	50 m	100 m	200 m	500 m
Triangle mesh	20.106	40.006	50.022	100.016	200.028	502.553
Mean distance difference	1.365	1.693	2.396	2.963	4.391	4.6931
Volume	38.191	58.981	68.912	116.219	218.512	519.312
Mean distance difference	18.191	18.981	18.912	16.219	18.512	19.312

Fig. 20(b) shows that there are similar classifications using two integrations resulting from different buffer analysis models. In Table 4, there are more numbers of voxels in the voxel-buffer classification. This verifies the findings of Sections 4.3.1 and 4.3.2 that the tri-buffer is more accurate with a higher goodness of fit.

5. Discussion

The 3D buffer irregular triangle buffer (ITB) algorithm introduced in this contribution can be used to calculate the buffer analysis presented by an irregular triangular mesh in 3D. It is, however, acknowledged that compared with the voxel method ($c3 \times O(N)$), generating a triangular-mesh 3D buffer is slow under many situations, in spite of our algorithm running close to the linear time. In order to determine specific situations, we compared curves of complexity between voxel model and triangular model, which is presented in Table 5 and Fig. 21.

Fig. 21 shows that less time is used by the block buffer method at any given time. Considering the computer's capacity and accuracy, the size of the cube of the signed Euclidean field is $20 \times 20 \times 20$ m. The method introduced in this manuscript took twice the time that the block method took, but this must be considered an acceptable trade-off considering the improvements in accuracy using an acceptable computer memory capacity to run the buffer analysis algorithm. For instance, when the buffer distance is less than 20 m, the block method has to use a smaller sized cube in order to maintain an acceptable accuracy, but the ITB method can still use a 20 m sized cube and remain accurate. This feature is obviously important since the geometric progressions do not become complicated and computer-memory 'hungry' with the need for smaller cube sizes.

Furthermore, the precision is a critical evaluation standard that verifies whether a methodology of buffer analysis is enough good to satisfy the mineral potential demands or not. The improved method discussed in this paper can be easily extended to satisfy more strict demands, and it can add a number of project points so that an irregular triangle mesh
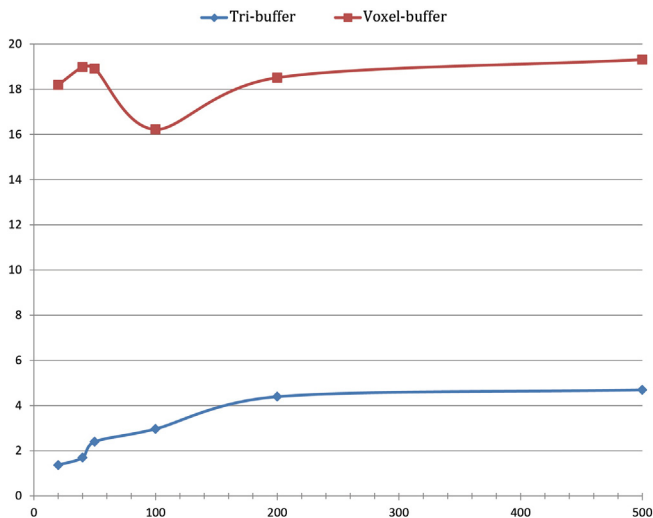
can be more accurate (refer to Section 3.4). In detail, we can divide triangles representing a geological object and calculate the project points using the new triangles. This is followed by applying the DSI algorithm to smooth the "reference surface" for the buffer analysis. However, the voxel methodology used for buffer analysis has a poor adaptation in this aspect. The only way for enhancing its precision is to vastly increase a number of voxels, but it is limited by computer's performance.

6. Conclusion and future work

This paper outlines an improved buffer analysis method that is implicit, precise and has triangulated characteristics. The method includes the four consecutive steps of: (1) voxelization of geological models; (2) improving 3D Euclidean distance transform and calculating the signed distance field; (3) extracting surfaces from the field; and (4) smoothing buffer surface based on the DSI algorithm (Fig. 1).

The innovation of this contribution is the reporting of an improved methodology of buffer analysis for prospectivity mapping with respecting to ore-deposit demands rather than describing an advance in methodology of surface rendering of "geological complexity".

Fig. 19. Mean distance difference. The X-axis represents buffer distance; Y-axis shows mean distance difference.
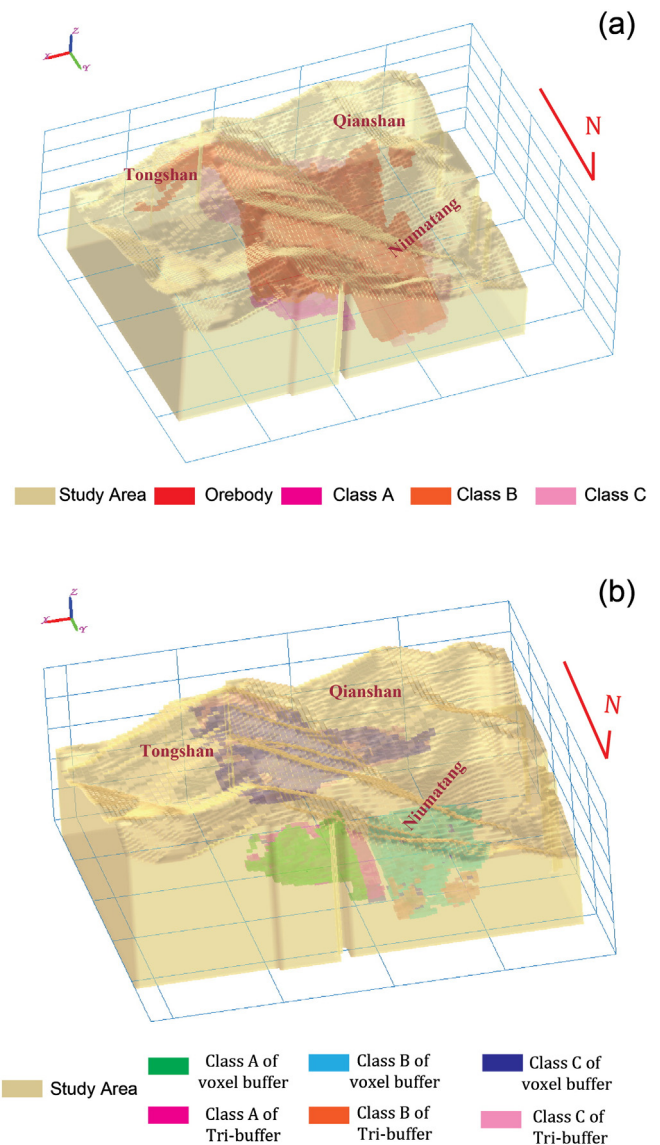
Fig. 20. Comparison of classification of weights-of-evidence: (a) classification using the voxel-buffer method; and (b) comparison of classifications.

Table 4
The number of voxels using different buffer methods.

	Class A, Poster possibility [>0.9]	Class B, Poster possibility [0.8, 0.9]	Class C, Poster possibility [0.6, 0.8]
Voxel-buffer	3527	2097	4572
Tri-buffer	3398	2013	4491

Table 5
Comparative consuming-time between the triangle- and voxel-buffers.

Buffer (m)	20	40	50	100	200	500
ITB method(s)	24.875	24.326	27.355	27.73	27.611	29.823
Block method(s)	12.253	13.822	14.443	14.885	15.031	16.661

Advantages of this method include: (1) triangle mesh buffer is more approximate to theoretical buffers without huge numbers of intersections, and the shape of triangle mesh depends on the buffer distance rather than size of voxel; (2) better visualized effect and much more details of B-Rep could be represented by irregular triangle mesh than voxel; (3) the buffer analysis time complexity is $T = c^* O(N)$, which means complexity is linear and the method has practicability; (4) the triangle mesh buffer uses less memory than a voxel buffer and, generally, without topology, each triangle is composed of three points in memory, while each voxel is represented by six points; (5) due to the reconstruction of a surface by algorithms with few interaction, models constructed using the method presented here is more renewable and updatable; (6) six examples and comparisons were carried out in Sections 4.2 and 4.3, which verified the above comment that the reliability of a triangle B-Rep buffer improves due to voxel buffering in aspects of visualization, goodness of fit, and the distance difference to a theoretical buffer body; and (7) the more exact a buffer is, the more useful is the geological influence domains created by it when mathematical functions integrate the domains as representative predictor models (Fig. 20).

In general, the models presented in this contribution can satisfy demands and improve the applied effects of buffer analysis on model-based mineral potential mapping. The buffer analysis method is especially suitable for extracting influent domains from contact metasomatic deposits, and the size of target is improved by improving the buffer analysis method.

Obviously, this models presented in this contribution will be improved with time through integration advantages in voxel- and irregular tri-buffer analyses, and it is here consider that the most important point of this continuously improving methodology is the topology of geometry. B-Rep body constructed by this method is not a topological model, which means that data structure of B-Rep body does not record topology, like common points, edges. Furthermore, although we compare mean distance difference between voxel-buffer and irregular tri-buffer, this paper do not versify how far distance difference is between irregular tri-buffer and buffer distance pointed by geologists at critical positions, for instance nodes on original surfaces. Nevertheless, considering that more wide-ranging applications are being used for GIS-based mineral potential mapping, such as spatial analysis calculation, implementation of topological surfaces will make these applications more effective, stable and user-friendly.

Conflict of interest

1. Emmanuel John M. Carranza works for James Cook University.

2. Laurent Ailleres works for the School of Earth, Atmosphere and Environment Faculty of Science, Monash University.

Acknowledgements

References

Agterberg, F., 1970. Multivariate prediction equations in geology. Math. Geol. 2, 319–324.
Agterberg, F., Bonham-Carter, G., Wright, D., 1990. Statistical Pattern Integration for Mineral Exploration. Pergamum Press, Oxford.
Agterberg, F., Bonham-Carter, G., Cheng, Q., Wright, D., 1993. Weights of evidence modeling and weighted logistic regression for mineral potential mapping. Comput. Geol. 25, 13–32.
Amenta, N., Choi, S., Kolluri, R.K., 2001. The power crust, unions of balls, and the medial axis transform. Comput. Geom.: Theory Appl. 19 (2–3), 127–153.
Bajaj, C.L., Bernardini, F., Xu, G., 1995. Automatic reconstruction of surfaces and scalar fields from 3d scans. ACM SIGGRAPTH 1995, Computer Graphics Proceedings. ACM Press, New York, NY, USA, pp. 109–118.
Bonham-Carter, G.F., 1994. Geographic Information Systems for Geoscientist: Modeling with GIS Oxford Elsevier. (398 pp.).
Bonham-Carter, G.F., Agterberg, F.P., 1989. Weights of evidence modelling: a new approach to mapping mineral potential. Geol. Surv. Can. 89, 171–183.
Brown, W.M., Gedeon, T.D., Groves, D.I., Barnes, R.G., 2000. Artificial neural networks: a new method for mineral prospectivity mapping. Aust. J. Earth Sci. 47, 757–770.
Calcagno, P., Chiles, J.P., Courrioux, G., Guillen, A., 2008. Geological modelling from field data and geological knowledge part I. Modelling method coupling 3D potential-field interpolation and geological rules. Phys. Earth Planet. Inter. 171, 147–157.
Cargill, S.M., Clark, A.L., 1978. Report on the activity of IGCP project 98. Math. Geol. 10, 411–417.
Carranza, E.J.M., 2004. Objective selection of suitable unit cell size in data-driven modelling of mineral prospectivity. Comput. Geosci. 35, 2032–2046.
Carranza, E.J.M., Sadeghi, M., 2010. Predictive mapping of prospectivity and quantitative estimation of undiscovered VMS deposits in Skellefte district (Sweden). Ore Geol. Rev. 38, 219–241.
Chen, Y., 2010. On epizonogenism and genetic classification of hydrothermal deposits. Earth Sci. Front. 17, 27–34 (China University of Geosciences, Peking University, Beijing).

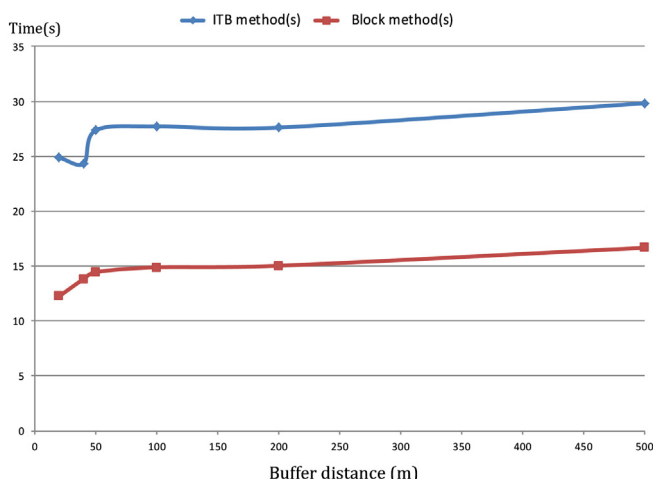
Fig. 21. Comparative consuming-time.

Chen, J., Wang, C., 2012. Three-dimensional metallogenic prediction in Yongmei region based on digital ore deposit model. Sci. Technol. Manag. Land Resour. 29, 14–20.

Chen, J., Lü, P., Wu, W., Zhao, J., Hu, Q., 2007. A 3D method for predicting blind ore-bodies based on a 3D visualization model and its application. Earth Sci. Front. 14, 54–62.

Cheng, Q.M., 2007. Mapping singularities with steam sediment geochemical data for prediction of undiscovered mineral deposits in Gejiu, Yunnan Province, China. Ore Geol. Rev. 32, 314–324.

Cheng, Q., Agterberg, F.P., 1999. Fuzzy weights of evidence method and its application in mineral potential mapping. Nat. Resour. Res. 8, 27–35.

Cheng, Q., Agterberg, F.P., Bonham-Carter, G.F., 1996. Fractal pattern integration for mineral potential estimation. Nat. Resour. Res. 5, 117–130.

Danielsson, P., 1980. Euclidean distance mapping. Comput. Graph. Image Proc. 14, 227–248.

Edelsbrunner, H., Mucke, E.P., 1994. Three-dimensional alpha shapes. ACM Trans. Graph. 13 (1), 43–72.

Ellul, C., Haklay, M., 2006. Requirements for topology in 3D GIS. Trans. GIS 10 (2), 157–175.

Feito, F., Torres, J.C., Urena, A., 1995. Orientation, simplicity and inclusion test for planar polygons. Comput. Graph. 19, 595–600.

Hoppe, H., DeRose, T., Duchamp, T., McDonald, J., Stuetzle, W., 1992. Surface reconstruction from unorganized points. Computer Graphics (Proceedings of ACM SIGGRAPH 92). ACM Press, New York, NY, USA, pp. 71–78.

Hou, N.K., Wu, L.X., 2002. An object-oriented three-dimensional topological data model based on component for geology modeling. Geom. Inform. Sci. Wuhan Univ. 27 (5), 467–472.

Hou, Z., Zhang, H., Pan, X., Yang, Z., 2011. Porphyry Cu (–Mo–Au) deposits related to melting of thickened mafic lower crust: examples from the eastern Tethyan metallogenic domain. Ore Geol. Rev. 39 (1), 21–45.

Hou, Z.Q., Yang, Z.M., Qu, X.M., Meng, X.J., Li, Z.Q., Beaudoin, G., Rui, Z.Y., Gao, Y.F., Zaw, K., 2009. The Miocene Gangdese porphyry copper belt generated during post-collisional extension in the Tibetan Orogen. Ore Geol. Rev. 36 (1–3), 25–51.

Houlding, S.M., 1994. Geoscience Modelling Computer Techniques for Geological Characterization. Spring ErVerlag, Berlin.

Lajaunie, C., Courrioux, G., Manuel, L., 1997. Foliation field and 3D cartography in geology: principles of a method based on potential interpolation. Math. Geol. 29, 571–584.

Li, F., Pan, M., Zhu, L., 2005. Research on the algorithm for 3D raster buffer-generation. J. Comp.-Aided Des. Comp. Graph. 17, 1928–1932.

Li, L., Zhao, Z.G., Guo, R.Z., 2012. 3D topological construction for spatial physical object. Geom. Inform. Sci. Wuhan Univ. 37 (6), 719–723.

Li, N., Wu, X., Xiao, K., Chen, X., 2013. Rapid voxelization method for complex orebody. J. Huazhong Univ. Sci Tech Nat. Sci. Ed. 41, 34–37.

Li, X.H., Yuan, F., Zhang, M.M., Jia, C., Jowitt, S.M., Ord, A., Zheng, T.K., Hu, X.Y., Li, Y., 2015. Three-dimensional mineral prospectivity modeling for targeting of concealed mineralization within the Zhonggu iron orefield, Ningwu Basin, China. Ore Geol. Rev. 71, 633–654.

Lin, H.-W., Wang, G., 2003. Three dimensional singed Euclidean distance transform and its applications. Chin. J. Comput. 26, 1645–1651.

Liu, Y.C., Luo, G.Y., 2008. Exploration Report of Fe Deposit in Daye Hubei, China. Wuhan Iron & Steel Group Minerals Co., Ltd.

Lorenesen, W.E., Cline, H.E., 1987. Marching cubes: a high resolution 3D surface construction algorithm. Comput. Graph. 21, 163–169.

Lu, X., Wang, H., 2012. An algorithm for 3D vector buffer based on efficient boolean operation. J. Chin. Univ. Min. Technol. 41, 481–487.

Lü, Q., Qi, G., Yan, J., 2013. 3D geologic model of Shizishan ore field constrained by gravity and magnetic interactive modelling: a case history. Geophysics 78 (1), B25–B35.

Malehmir, A., Thunehed, H., Tryggvason, A., 2009. The Paleoproterozoic Kristineberg mining area, northern Sweden: results from integrated 3D geophysical and geological modelling, and implications for targeting ore deposits. Geophysics 74 (1), B9–B22.

Mallet, J.L., 1997. Discrete modeling for natural objects. Math. Geol. 29, 199–219.

Mallet, J.L., 2003. Geomodelling. Applied Geostatistics. Oxford University Press, pp. 1–10.

Mao, X.C., Tang, Y.H., Deng, H., 2012. Three-dimensional morphological analysis method for geologic bodies and its application. J. Cent. South Univ., Sci. Technol. 43 (2), 588–595.

Perrouty, S., Aillères, L., Jessell, M., Baratoux, L., Bourassa, Y., Crawford, B., 2012. Revised Eburnean geodynamic evolution of the gold-rich southern Ashanti Belt, Ghana, with new field and geophysical evidence of pre-Tarkwaian deformations. Precambrian Res. 204–205, 12–39.

Perrouty, S., Lindsay, M.D., Jessell, M.W., Aillères, L., Martin, R., Bourassa, Y., 2014. 3D Modeling of the Ashanti Belt, Southwest Ghana: Evidence for a Litho-Stratigraphic Control on Gold Occurrences Within the Birimian Sefwi Group 63. pp. 252–264.

Porwal, A., Carranza, E.J.M., 2001. Extended weights of evidence modelling for predictive mapping of base metal deposit potential in Aravalli Province, western India. Explor. Min. Geol. 10, 273–287.

Porwal, A., Carranza, E.J.M., 2015. Introduction to the special issue: GIS-based mineral potential modelling and geological data analyses for mineral exploration. Ore Geol. Rev. 70, 477–483.

Porwal, A., Hale, M., 2000. GIS-based weights-of-evidence analysis of multi-class spatial data for predictive mineral mapping: a case study from Aravalli Province, western India. Proceedings, XIV International Conference on Applied Geologic Remote Sensing, pp. 377–384.

Porwal, A., Carranza, E.J.M., Hale, M., 2006. A hybrid fuzzy weights-of-evidence model for mineral potential mapping. Nat. Resour. Res. 15, 1–14.

Porwal, A., Gonzalez-Alvarez, I., Markwitz, V., McCuaig, T., Mamuse, A., 2010. Weights-of-evidence and logistic regression modelling of magmatic nickel sulphide prospectivity in the Yilgarn Craton, Western Australia. Ore Geol. Rev. 38, 184–196.

Schneider, M., Behr, T., 2006. Topological relationships between complexes spatial objects. Non-renew. Resour. 31, 39–81.

Singer, D.A., 1993. Basic concepts in three-part quantitative assessments of undiscovered mineral resources. Non-renew. Resour. 2 (2), 69–81.

Singer, D.A., 2006. Typing mineral deposits using their associated rocks, grades and tonnages using a probabilistic neural network. Math. Geol. 38, 465–474.

Singer, D.A., Menzie, W., 2010. Quantitative Mineral Resource Assessments: An Integrated Approach. Oxford University Press (232 pp.).

Tang, J., Wang, D.-H., Wang, X., Zhong, K., Ying, L., Zheng, W., Li, F., Guo, N., Qin, Z., Yao, X., Li, L., Wang, Y., Tang, X., 2010. Geological features and metallogenic model of the Jiama copper-polymetallic deposit in Tibet. Acta Geosci. Sin. 31, 495–506.

Tang, J.X., Deng, S.L., Zheng, W.B., 2011. An exploration model for Jiama copper polymetallic deposit in Maizhokunnger County, Tibet. Mineral Deposits 30, 179–195.

Tang, J.X., Wang, D.H., Wang, X., Zhong, K., 2009. Exploration Report of Copper-Polymetallic Deposit, Jiama, MoZhuGongKa District, Tibet, China. Office of Land and Resources in Tibet, Lhasa.

Tangestani, M.H., Moore, F., 2001. Porphyry copper potential mapping using the weights-of evidence model in a GIS, northern Shahr-e-Babak, Iran. Aust. J. Earth Sci. 48, 695–701.

Treece, G.M., 1999. Regularised marching tetrahedral: improved iso-surface extraction. Comput. Graph. 23, 583–598.

Wang, S.C., 1999. Mineral Resources Assessment Methods. Geological Publish House, Beijing (219 pp.).

Wang, G., Zhang, S., Yan, C., 2011. Mineral potential targeting and resource assessment based on 3D geological modelling in Luanchuan region, China. Comput. Geosci. 37, 1976–1988.

Wang, C.M., Deng, J., Emmanuel John, M.C., Santosh, M., 2014a. Tin metallogenesis associated with granitoids in the north-western Sanjiang Tethyan domain: nature, deposit types, and tectonic setting. Gondwana Res. 26 (2), 576–593.

Wang, C.M., Deng, J., Emmanuel John, M.C., Lai, X.R., 2014b. Nature, diversity and temporal–spatial distributions of sediment-hosted Pb–Zn deposits in China. Ore Geol. Rev. 56 (1), 327–351.

Wang, C.M., Zhang, D., Wu, G.G., Santosh, M., Zhang, J., Xu, Y.G., Zhang, Y.Y., 2014c. Geological and isotopic evidence for a magmatic–hydrothermal origin of the Ag–Pb–Zn deposits in the Lengshuikeng district, east-central China. Mineral. Deposita 49 (6), 733–749.

Wang, C.M., Deng, J., Lu, Y.J., Leon, B., Kemp, A.I.S., Campbell McCuaig, T., 2015a. Nature and origin of Ordovician Zhibenshan granite from the Baoshan terrane in the Sanjiang region and its significance for understanding proto-Tethys evolution. Int. Geol. Rev. 57 (15), 922–1939.

Wang, C.M., Deng, J., Santosh, M., Campbell McCuaig, T., Lu, Y.J., Emmanuel, J.M.C., Wang, Q.F., 2015b. Age and origin of the Bulangshan and Mengsong granitoids and their significance for post-collisional tectonics in Changming–Menglian Paleo-Tethys Orogen. J. Asian Earth Sci. 113 (2), 656–676.

Wu, H., 1997. Problem of buffer zone construction in GIS. J. Wuhan Tech. Univ. Surv. Mapp. 22, 358–364.

Wu, L., Lü, Y., 2001. Geographic Information System — Theory, Method and Application. Science Press Ltd., Beijing (466 pp.).

Wu, H., Gong, J., Li, D., 1999. Buffer curve and buffer generation algorithm in aid of edge-constrained triangle network. Acta Geod. Cartograph. Sin. 28, 355–359.

Xiao, K., Li, N., Sun, L., Zou, W., Li, Y., 2012. Large scale 3D mineral prediction methods and channels based on 3D information technology. J. Dizhixuekan 36, 229–236.

Xiao, K., Li, N., Porwal, A., Holden, E.J., Bagas, L., Lu, Y.J., 2015. GIS-based 3D prospectivity mapping: a case study of jiama copper-polymetallic deposit in Tibet, China. Ore Geol. Rev. 71, 611–632.

Ye, Q.Z., 1988. The signed Euclidean distance transform and its applications. Proceedings of 9th International Conference of Pattern Recognition, Rome, Italy, pp. 495–499.

Ying, L.J., Wang, C.H., Tang, J.X., Wang, D.H., Qu, W.J., Li, C., 2014. Re-Os systematics of sulfides (chalcopyrite, bornite, pyrite and pyrrhotite) from the Jiama Cu-Mo deposit of Tibet, China.

Yuan, F., Li, X.H., Zhang, M.M., Jowitt, S., Jia, C., Zheng, T.K., Zhou, T.F., 2014. Three-dimensional weights of evidence-based prospectivity modelling: a case study of Baixiangshan mining area, Ningwu Basin, middle and lower Yangze metallogenic belt, China. J. Geochem. Explor. 145, 82–97.

Zhang, H., Wen, Y., 2006. Fundamental Algorithms in Geographic Information System. Beijing Science Press, pp. 185–199.

Zhang, D., Cheng, Q., Zuo, R., 2013. A comparison of two different unit division methods in weights of evidence. J. Jilin Univ. (Earth Sci. Ed.) 43, 1040–1052.

Zheng, W.B., 2012. The Study on Metallogenic Model and Prospecting Pattern for Jiama Polymetallic Copper Deposit, Tibet, China. PhD, CAGS.

Zhao, P., 2002. "Three-component "quantitative resource prediction and assessment: theory and practice of digital mineral prospecting. Earth Sci. Jo. China Univ. Geosci. 27, 48–489.

Zhao, P., 2007. Quantitative mineral prediction and deep mineral exploration. Earth Sci. Front. 14, 1–10.

Zhao, P., Chen, J., Zhang, S., 2003. The new development of "three components" quantitative mineral prediction. Earth Sci. J. China Univ. Geosci. 10, 455–463.

Zhu, Y.S., 1997. Prospectivity Mapping Methods. Geological Publish House, Beijing.

Zlatanova, S., Rahman, A.A., Shi, W., 2004. Topological models and frameworks for 3D spatial objects. Comput. Geosci. 30, 419–428.

Zuo, R.G., Cheng, Q.M., Agterberg, F.P., 2009. Application of a hybrid method combining multilevel fuzzy comprehensive evaluation with asymmetric fuzzy relation analysis to mapping prospectivity. Ore Geol. Rev. 35, 101–108.